



HAL
open science

Self-assembly of dodecagonal and octagonal quasicrystals in hard spheres on a plane

Etienne Fayen, Marianne Impéror-Clerc, Laura Filion, Giuseppe Foffi, Frank Smallenburg

► **To cite this version:**

Etienne Fayen, Marianne Impéror-Clerc, Laura Filion, Giuseppe Foffi, Frank Smallenburg. Self-assembly of dodecagonal and octagonal quasicrystals in hard spheres on a plane. *Soft Matter*, 2023, 10.1039/D3SM00179B . hal-04047663

HAL Id: hal-04047663

<https://hal.science/hal-04047663v1>

Submitted on 27 Mar 2023

HAL is a multi-disciplinary open access archive for the deposit and dissemination of scientific research documents, whether they are published or not. The documents may come from teaching and research institutions in France or abroad, or from public or private research centers.

L'archive ouverte pluridisciplinaire **HAL**, est destinée au dépôt et à la diffusion de documents scientifiques de niveau recherche, publiés ou non, émanant des établissements d'enseignement et de recherche français ou étrangers, des laboratoires publics ou privés.

Cite this: DOI: 00.0000/xxxxxxxxxx

Self-assembly of dodecagonal and octagonal quasicrystals in hard spheres on a plane

Etienne Feyen^a, Marianne Impéror-Clerc^a, Laura Filion^b, Giuseppe Foffi^a, and Frank Smallenburg^a

Received Date

Accepted Date

DOI: 00.0000/xxxxxxxxxx

Hard spheres are one of the most fundamental model systems in soft matter physics, and have been instrumental in shedding light on nearly every aspect of classical condensed matter. Here, we add one more important phase to the list that hard spheres form: quasicrystals. Specifically, we use simulations to show that an extremely simple, purely entropic model system, consisting of two sizes of hard spheres resting on a flat plane, can spontaneously self-assemble into two distinct random-tiling quasicrystal phases. The first quasicrystal is a dodecagonal square-triangle tiling, commonly observed in a large variety of colloidal systems. The second quasicrystal has, to our knowledge, never been observed in either experiments or simulations. It exhibits octagonal symmetry, and consists of three types of tiles: triangles, small squares, and large squares, whose relative concentration can be continuously varied by tuning the number of smaller spheres present in the system. The observed tile composition of the self-assembled quasicrystals agrees very well with the theoretical prediction we obtain by considering the four-dimensional (lifted) representation of the quasicrystal. Both quasicrystal phases form reliably and rapidly over a significant part of parameter space. Our results demonstrate that entropy combined with a set of geometrically compatible, densely packed tiles can be sufficient ingredients for the self-assembly of colloidal quasicrystals.

1 Introduction

Hard spheres are arguably the most fundamental model system in colloid science. The colloidal equivalent of marbles, hard spheres only interact when colliding, but despite this simplicity exhibit nearly all important aspects of phase behavior. As such, colloidal hard spheres have been instrumental in enhancing our understanding of crystal nucleation^{1,2}, crystallization in confinement^{3–9}, two-dimensional melting^{10,11}, glassy dynamics^{12–16}, crystal defects^{17–19}, among many others. Their important role in soft matter science stems from their theoretical simplicity, which makes them a natural first approximation for particles with a hard core, as well as the fact that they can be quantitatively reproduced in the lab^{20–23}. One aspect of colloidal phase behavior where hard spheres have thus far not proven suitable as a model sys-

tem is the formation of quasicrystals. These exotic structures possess long-range order but lack periodicity and typically exhibit so-called "forbidden" symmetries, incompatible with periodic crystalline order. They have been predicted to form or directly observed in a variety of soft-matter systems consisting of nanoparticles or macromolecules^{24–27}, as well as in several (non-additive) 2D binary Lennard-Jones mixtures^{28–31}, but have so far remained elusive in colloidal particles on the micrometer scale.

This is unfortunate, as such a colloidal model system that reliably forms quasicrystals would be ideal for the real-time study of quasicrystal self-assembly. In computer simulations of colloidal soft matter, quasicrystals are typically found in systems with highly specific interactions – such as oscillatory potentials, patchy interactions, and square-shoulder repulsion^{24,32–37} – which are hard to realize in the lab. While complex quasicrystal approximants have been found to self-assemble in simulations of polydisperse mixtures of hard spheres³⁸, and finite clusters with icosahedral symmetry have been shown to form in spherical confinement^{3,4,39}, to date hard-sphere systems have not been found to be capable of forming a quasicrystal.

Here, we demonstrate quasicrystal self-assembly in binary mixtures of hard spheres lying on a flat plane. In particular, we find that this simple, purely entropic quasi-two-dimensional system exhibits an amazingly rich self-assembly behavior, forming

^a Université Paris-Saclay, CNRS, Laboratoire de Physique des Solides, 91405 Orsay, France

^b Soft Condensed Matter, Debye Institute for Nanomaterials Science, Utrecht University, Utrecht, Netherlands

† Electronic Supplementary Information (ESI) available: [details of any supplementary information available should be included here]. See DOI: 10.1039/cXsm00000x/

‡ Additional footnotes to the title and authors can be included e.g. 'Present address:' or 'These authors contributed equally to this work' as above using the symbols: ‡, §, and ¶. Please place the appropriate symbol next to the author's name and include a ¶footnotetext entry in the the correct place in the list.

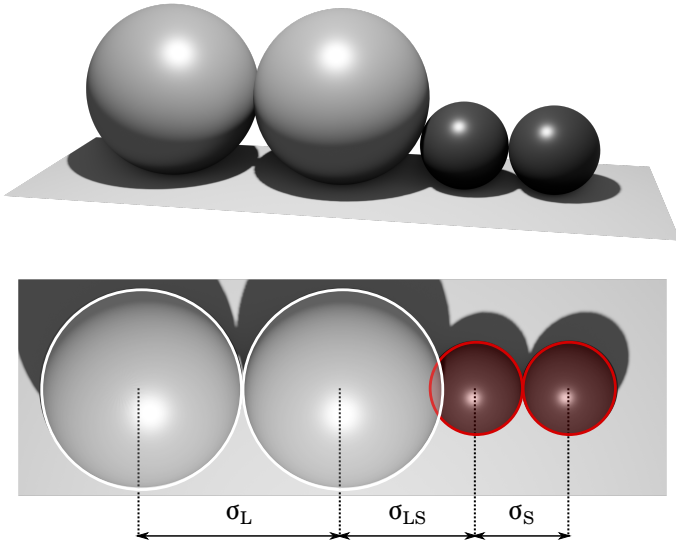


Fig. 1 Schematic depiction of the model. 3D hard spheres lying on a flat surface (top) can be interpreted as an equivalent 2D system of non-additive hard disks (bottom). Spheres of the same type behave like standard hard disks (their projections cannot overlap), while the closest projected distance between particles of different types σ_{LS} is smaller than the sum of the radii.

not only six periodic crystal phases, but two random-tiling quasicrystals as well: one dodecagonal and one octagonal. Although dodecagonal quasicrystals are relatively common in soft matter models^{25,32,33,40–42}, octagonal ones are much more rare^{33–36}. Moreover, unlike previously observed eight-fold quasicrystals made up of two tiles, the octagonal tiling we observe here is composed of three distinct tiles, whose relative composition can be directly tuned by changing the fraction of small spheres in the system. Both quasicrystal phases form reliably and rapidly over a significant part of parameter space. As binary hard spheres on a plane are directly experimentally realizable, to the point where they quantitatively match simulations^{10,43}, this discovery identifies an ideal model system for studying essentially all properties of quasicrystals, including their structure, nucleation, melting, and defect dynamics.

2 Model

We consider mixtures of hard spheres of two different sizes constrained to lie on a flat plane. As illustrated in Fig. 1, this system can be mapped onto an equivalent 2D one by looking at its projection on the substrate, where spheres become disks. As the particles are constrained to move in only two dimensions, the disks corresponding to spheres of equal size cannot overlap, and hence interact simply as hard disks. However, for spheres of different sizes, a small amount of overlap of the 2D projections of the particles is allowed. Specifically, the distance of closest approach between the projections of a large particle of diameter σ_L and a small particle of diameter σ_S is given by the geometric mean of their diameters $\sigma_{LS} = \sqrt{\sigma_L \sigma_S}$.

The phase behavior of a mixture of N_L large spheres and N_S small spheres confined to a substrate with area A is controlled by three parameters: the size ratio $q = \sigma_S/\sigma_L$, the fraction of

small spheres $x_S = N_S/(N_L + N_S)$, and the packing fraction $\eta = (N_S \sigma_S^2 + N_L \sigma_L^2) \pi / 4A$ occupied by the equivalent 2D disks. Note that since some overlap is allowed between different species in the 2D projection, the total packing fraction may exceed 1 in some cases.

3 Infinite pressure phase behavior

Even for simple binary mixtures in 2D, the number of different ordered structures that can emerge can be quite large and difficult to enumerate. To obtain an impression of the crystals we might expect to find, we used a technique specifically designed to detect the close-packing crystal structures that would form in the limit of infinite pressure. To this end, we followed Ref. 44 to map out the infinite pressure phase diagram of non-additive hard disks. Specifically, for a range of size ratios and compositions, we construct a library of candidate crystal structures and find – for each combination of q and x_S – the best-packed phase or coexistence of phases. Note that in the notation of Ref. 44, the present case of spheres lying on a flat plane corresponds to a size-ratio-dependent non-additivity parameter

$$\Delta(q) = 2\sqrt{q}/(1+q) - 1, \quad (1)$$

such that the contact distance between a small and a large sphere can be written as

$$\sigma_{LS} = (1 + \Delta) \frac{\sigma_L + \sigma_S}{2}. \quad (2)$$

For each size ratio, we use the data from Ref. 44 for the best packed candidate structures, which were obtained from systematic sampling of unit cells containing up to 12 particles using Monte Carlo simulations with a variable box shape⁴⁶. The infinite pressure phase diagram is then constructed from these structures by common-tangent construction⁴⁴, and shown in Fig. 2.

In addition to the trivial monodisperse hexagonal crystal phases of the large or small particles (Hex_L and Hex_S, respectively), we observe a wide variety of binary phases. Since any pure crystal phase can only occur at a single composition x_S , the densest-packed state at most points in the phase diagram (white regions) is a coexistence between two crystal phases at different compositions: the ones appearing directly above and below the chosen state point. In addition to the expected monodisperse hexagonal crystals of either large or small particles, we find a variety of binary crystal phases, many of which are similar to those found in additive systems^{44,45}. Note that for large size ratios, the system becomes almost additive. In the additive case, it is proven that there exist no denser structures than a coexistence of Hex_L and Hex_S for $q \gtrsim 0.74$ ⁴⁷. Therefore we expect no additional binary crystal phases to appear at size ratios above our investigated range $0.3 \leq q \leq 0.75$.

For each phase in Fig. 2 we also depict the repeating unit that can be used to construct the crystal phase, which we call a tile. Unlike a unit cell, tiles can appear in the full crystal structure in multiple orientations. Interestingly, for certain coexistence regions, the two coexisting phases consist of tiles that can mix. One realization of this occurs at low size ratios ($q \simeq 0.3$) where the T1 and Hex_L phases consist of identical triangles of large particles, but decorated differently by small particles. In the region where

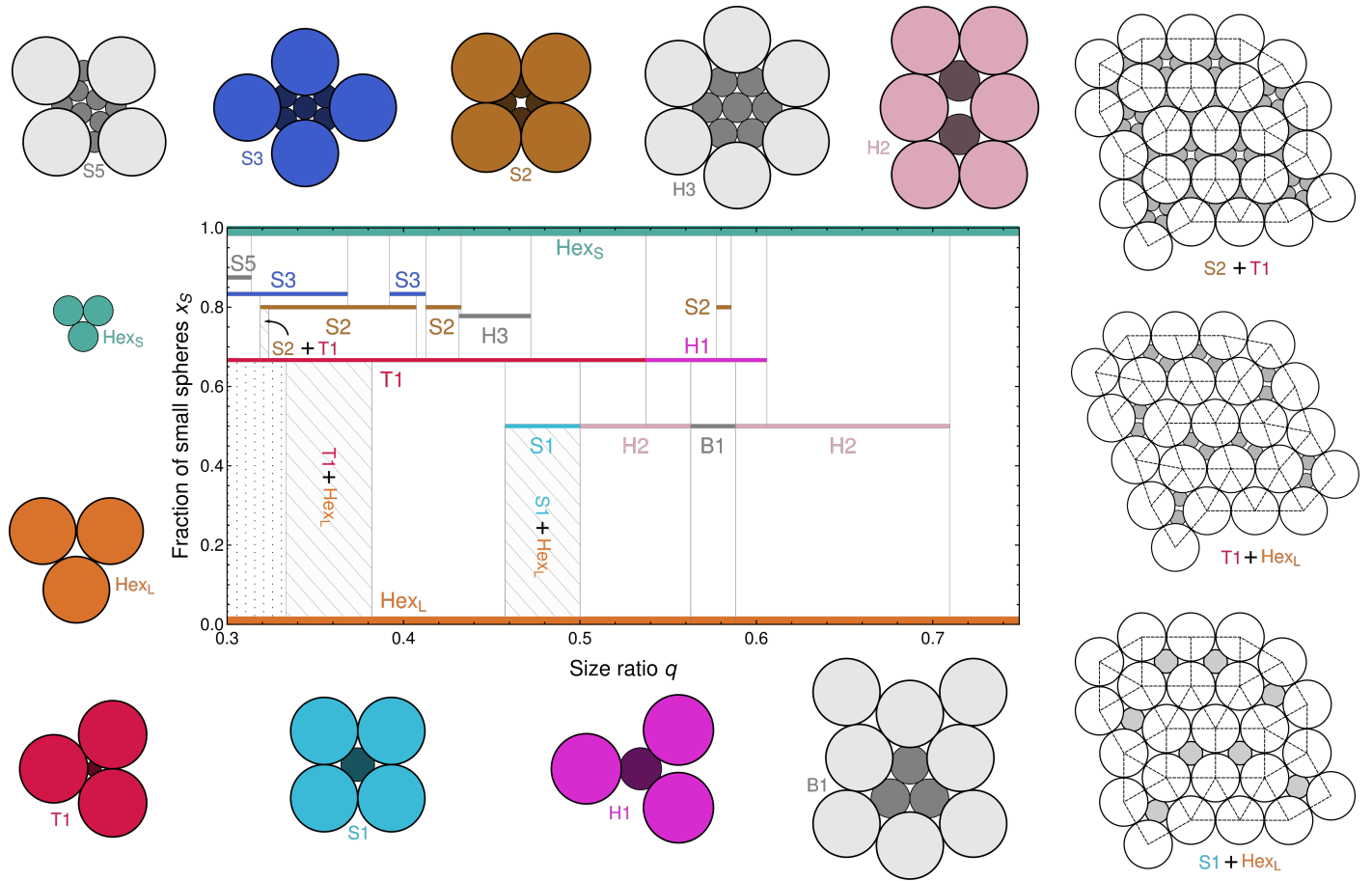


Fig. 2 Infinite-pressure phase behavior of binary mixtures of spheres on a flat plane, as a function of the size ratio q and fraction of small particles x_S . Phases are labeled following the naming scheme of Refs. 44,45. The white regions correspond to coexistence regions between the phases directly above and below. The striped and dotted areas indicate regions where these two phases can form random tilings or a lattice gas, respectively. Examples of finite patches of the three possible random tilings, corresponding to the striped regions in the diagram, are displayed on the right.

these two phases mix, they can form a lattice gas where tiles of T1 and Hex_L are randomly mixed (dotted region in Fig. 2). Another, much more interesting situation occurs when two tiles of different shapes can mix. This occurs in the three striped regions in Fig. 2. For example, at size ratios just below $q = 0.5$, the square tile of the S1 phase has the same edge length as the triangular tile of the Hex_L phase, allowing them to mix and form a space-filling square-triangle tiling^{44,45}, illustrated in the bottom right of Fig. 2. As this mixing increases the entropy without lowering the packing fraction, the expected phase at infinite pressure here is a random tiling of squares and triangles, which at an ideal composition $x_S = (3 - \sqrt{3})/4 \simeq 0.317$ is known to have 12-fold symmetry on average^{48,49}. Two closely related tilings, also illustrated in Fig. 2 are found at lower size ratios. As a result, one intriguing prediction from Fig. 2 is the possibility of a 12-fold quasicrystal self-assembling from simple binary mixtures of colloidal spheres on a substrate.

4 Finite pressure self-assembly

In practice, the infinite-pressure phase behavior is not a reliable indication for the phases one might find in a real self-assembly experiment. Self-assembly in a colloidal system takes place at finite

pressure, where particles can diffuse to reach their lattice site and vibrate around it. This brings vibrational entropy contributions to the free energy of different crystal phases which can fundamentally change the phase behavior. Moreover, dynamical arrest or competition with other candidate phases can prevent the reliable formation of a crystal even if it is thermodynamically stable.

Hence, for a more realistic look at the self-assembly, we perform computer simulations at finite pressure for an extensive grid of state points spanning size ratios $0.25 \leq q \leq 0.75$, compositions $0.05 \leq x_S \leq 0.95$, and packing fractions $0.7 \leq \eta \leq 1.0$. In particular, we run event-driven molecular dynamics (EDMD) simulations⁵⁰ in the canonical ensemble, i.e. at constant number of particles N , volume V , and temperature T . The simulation algorithm is an adaptation of the methods described in Ref. 51. We perform the EDMD simulations in the microcanonical ensemble, i.e. at constant number of particles N , volume V , and energy E . Initial configurations are obtained by starting in a dilute state at the desired composition, and then performing an EDMD simulation in which the particle diameters grow until the desired packing fraction is reached.

We perform a systematic exploration of parameter space for systems of $N = 2000$ particles, varying the composition x_S between

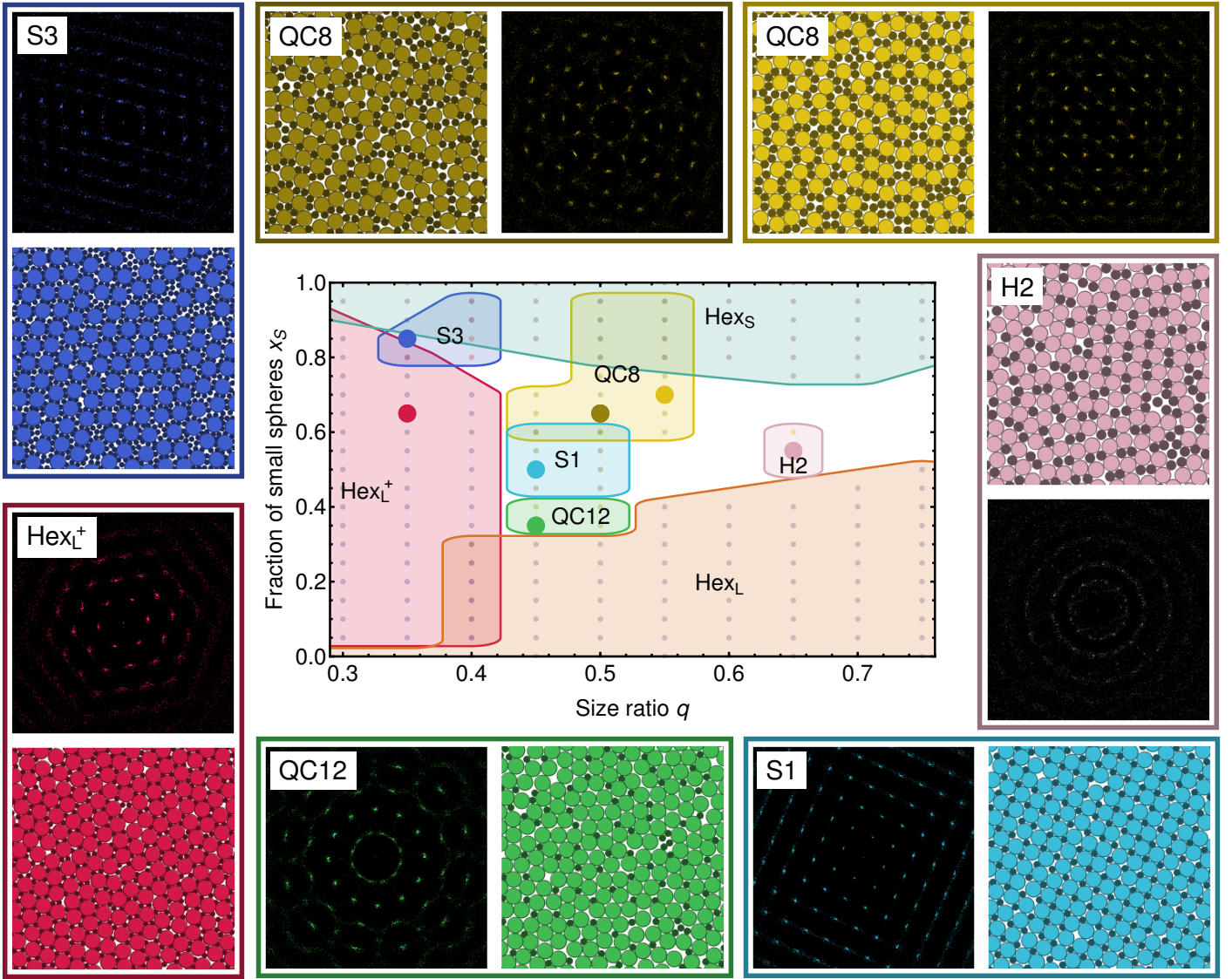


Fig. 3 Self-assembly diagram for binary mixtures of spheres on a flat plane, as a function of the size ratio q and fraction of small particles x_S . For each combination of q and x_S , we perform simulations at a range of different packing fractions, and report the observed phases. Points in the phase diagram contained in a colored region display the self-assembly of the corresponding phase. For each binary crystal phase, we include a representative snapshot (marked as a large dot of the corresponding phase color) and the scattering pattern that results from a Fourier transform of the positions of the large spheres. For the QC8 phase, we include two snapshots: one containing a large concentration of S1 squares (top middle) and one containing a large concentration of S2 squares (top right). Hex_L and Hex_S are hexagonal crystals consisting of only large or small spheres, respectively, and are not depicted. Note that at some state points, we find the self-assembly of two different phases that are either in coexistence or occur at different packing fractions – hence some of the crystal regions overlap. At state points without an indicated crystal phase, no crystallization was observed at any of the investigated packing fractions

0.05 and 0.95 in steps of 0.05 and the size ratio q between 0.25 and 0.75 in steps of 0.05. The packing fraction η ranged from 0.7 to up to 1.0 in steps of 0.01, where we only considered state points where the growing-particle simulations were able to rapidly reach the desired packing fraction without jamming. In other words, we assume that at packing fractions where jamming occurs during our initial compression, the system would likely be too densely packed to observe self-assembly on a reasonable time scale. Each self-assembly simulation is allowed to run for at least $10^6 \tau_{\text{MD}}$, with $\tau_{\text{MD}} = \sqrt{m\sigma_L^2/k_B T}$ the simulation time unit, m the mass of a particle (chosen equal for both species), σ_L the large-particle

diameter, and k_B Boltzmann's constant. Subsequently, longer simulations were performed for state points where self-assembly was considered likely to occur on a reasonable time-scale based on the final pressure of the first simulations. In particular, we extended the simulations at state points with a pressure $16 \lesssim P\sigma_L^2/k_B T \lesssim 33$ to a total length of $5 \cdot 10^6 \tau_{\text{MD}}$.

Our results are summarized in Fig. 3. The central diagram reports for each investigated combination of q and x_S what ordered phases were observed. We consider a crystal to have self-assembled for a given combination of q and x_S when we find significant clusters of the crystal in the simulation box for at least

one packing fraction. Our simulations show that a number of the best-packed phases we predicted in Fig. 2 indeed spontaneously self-assemble. Naturally, this includes the trivial hexagonal crystals of the large and small spheres (Hex_L and Hex_S) that can be found at compositions close to $x_S = 0$ and 1, respectively. Additionally, we observe large-scale crystallization into the S1 and S3 phases close to the regions expected from Fig. 2. We also observe the more complex H2 phase, albeit only in finite clusters – a closer inspection of the systems where these form show a very low overall mobility of the system, suggesting that crystallization of this phase is hindered by slow dynamics. For sufficiently low q , the system nearly always forms a hexagonal lattice of large spheres, with the small spheres interspersed between them (labeled Hex_S^+). Depending on the composition, this may look similar to the T1 phase (as depicted in the sample snapshot in Fig. 3), but the number of small spheres per triangular cavity in the lattice of large spheres appears to continuously depend on the composition x_S (see SI). For $x_S < 2/3$, this simply means that a random selection of the triangular holes are empty, resulting in a lattice gas or interstitial solid solution^{44,45}. For larger x_S , progressively more small particles are included between the large spheres, but we observe no clear structural transition between these regimes. Hence, we choose to collectively indicate this region as Hex_S^+ .

Most intriguingly, in addition to these periodic phases, we also observe the self-assembly of two distinct quasicrystals, both at size ratios between $q = 0.45$ and $q = 0.55$. The dodecagonal quasicrystal (QC12) that appears at low fractions of small spheres is indeed the square-triangle tiling^{48,49} expected from the infinite-pressure diagram. It is made of regular squares and triangles (S1 and Hex_L tiles). This quasicrystal is analogous to a number of quasicrystals observed in soft matter systems, including patchy particles with five attractive patches³², hard disks with a square-shoulder repulsion^{40,41}, binary mixtures of nanoparticles²⁵, block copolymers^{26,27}, and soft repulsive colloids³³. Additionally, various 3D systems have been shown to form quasicrystals consisting of layers of a square-triangle tiling^{42,52,53}. The second quasicrystal (QC8) has octagonal symmetry, and consists of a mixture of three tiles: the isosceles triangles that appear in the H1 phase, the squares from the S1 lattice, and the larger squares from the S2 lattice.

For the quasicrystals, local crystalline order is typically hard to see by eye, and we instead rely on the symmetry of the scattering pattern for our classification. In particular, for each simulation, we measured the two-dimensional structure factor of the final configuration using

$$S(\mathbf{k}) = \frac{1}{N} \left| \sum_{n=1}^N \exp(i\mathbf{k} \cdot \mathbf{r}_n) \right|^2. \quad (3)$$

where \mathbf{k} is a wave vector commensurate with the periodic simulation box, and \mathbf{r}_n is the position of particle n . We plot the resulting scattering pattern $S(\mathbf{k})$ in two dimensions via a logarithmic color scale. The resulting scattering patterns for selected state points are included in Fig. 3. Note that in the Supplemental Data, we include a full catalogue of all final configurations and their diffraction patterns.

5 Quasicrystal analysis

In order to examine the QC12 and QC8 quasiperiodic structures in more detail, we perform additional simulations of $N = 10000$ particles in the regime where they are found to self-assemble. In the final configurations, we reconstruct the underlying tiling from the bond network (see SI) and use it to analyse the quasicrystals.

In Fig. 4, we show portions of the final state of three simulated mixtures of 10^4 particles, at different state points: one corresponding to the QC12 phase and two corresponding to the QC8 phase. Note that the two QC8 snapshots consist primarily of the same three tiles, but mixed in different concentrations. The first is dominated by small squares, while the second, which contains more small particles, predominantly contains large squares. Nonetheless, both systems possess global octagonal symmetry as indicated by the diffraction patterns. The analysis of the tile orientations shows that in all three quasicrystal phases, tiles of the same shape occur in all possible orientations roughly with the same frequency, which is a common feature of random-tiling quasicrystals⁴⁹.

All three quasicrystal configurations shown in Fig. 4 also contain local patches of periodic structures, such as square or hexagonal regions, which may compete with the quasicrystal phase in stability. However, we never observe long-term growth of these patches. Instead, over the course of the corresponding simulations, such patches are regularly formed and destroyed as defects or fluid regions diffuse through the system.

For a defect-free dodecagonal square-triangle quasicrystal, it is well-known that half of the total system area should be occupied by squares, and the other half by triangles^{49,54}. In other words, $\sigma = \tau = 1/2$, where σ is the area fraction occupied by squares, and τ is the area fraction occupied by triangles. Ignoring the defects that inevitably arise during our self-assembly process, the QC12 configuration shown in Fig. 4 corresponds to $\sigma = 0.491$ and $\tau = 0.509$. Given both the presence of defects and the periodic boundary conditions of our finite system, this is fully consistent with random quasicrystalline order.

For the QC8 phase, it is less obvious what tile concentrations we should expect in a perfect random quasicrystal. As illustrated in the center and right panels of Fig. 4, the relative concentrations of the different tiles we find in the self-assembled QC8 phase vary drastically as a function of the fraction of small spheres in the system. Since the S2 squares contain 4 small particles each, while the S1 squares only contain a single small sphere, higher compositions x_S favor a larger concentration of S2 squares. For high x_S , the QC8 tiling consists almost purely of large S2 squares and H1 triangles, with the triangles joined in pairs that form a thin rhombus. In this limit, the tiling can be seen as a mixture of just two types of tiles – square and rhombic – that are identical to the tiles that form e.g. the Ammann-Beenker^{55,56} and Watanabe-Ito-Soma⁵⁷ octagonal aperiodic tilings. The same tiling – with different decorations of the tiles with particles – was previously observed in simulations of soft colloids³³, particles with an oscillating interaction potential^{34,36}, and patchy particles³⁵. However, to our knowledge, no octagonal quasicrystals have yet been observed to spontaneously self-assemble in soft-matter experiments.

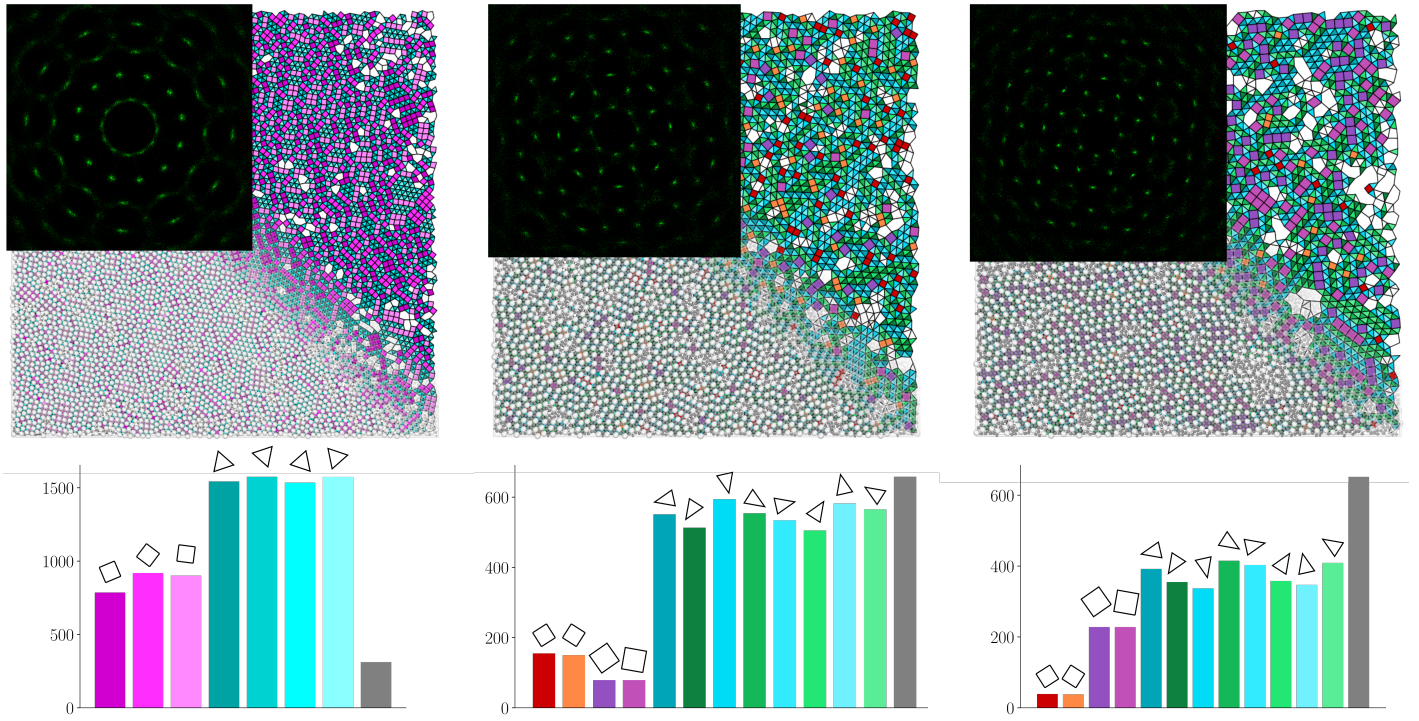


Fig. 4 Self-assembled dodecagonal and octagonal random-tiling quasicrystals in mixtures of 10^4 spheres on a flat plane, at state points (Left QC12) $q = 0.45$, $x_S = 0.35$, $\eta = 0.84$, (Middle QC8) $q = 0.5$, $x_S = 0.675$, $\eta = 0.86$ and (Right QC8) $q = 0.55$, $x_S = 0.725$, $\eta = 0.84$. The underlying tilings are highlighted and tiles colored according to shape and orientation. The insets show the diffraction patterns, signaling the global 12 or 8-fold symmetries. Tile distributions (Bottom) show the number of tile in each orientation in the tiling. The grey rightmost bar labeled denotes all defects.

In contrast, at low x_S the quasicrystal approaches a tiling of only H1 triangles and small S1 squares. Interestingly, a closely related tiling where the isosceles triangles are slightly deformed (breaking the 8-fold symmetry), was recently conjectured to be the densest-packed structure for a ternary mixture of hard disks⁵⁸. Our findings suggest that a new QC8 quasicrystal made of these two tiles - isosceles triangles and small squares - should exist, along with a whole family of three-tile QC8 structures at different compositions. In this respect, our results exhibit completely new types of aperiodic octagonal tilings, which, to the best of our knowledge, have not yet been described in the literature.

It is interesting to consider under what conditions the QC8 tiling observed here can exhibit true 8-fold symmetry. Counting different orientations, this tiling consists of 12 different tiles: 2 orientations of large squares, 2 orientations of small squares, and 8 differently oriented isosceles triangles. In general, quasicrystal vertices can be seen as a projection of a high-dimensional lattice into a lower dimensional space⁵⁴. As outlined in Ref. 49, this representation can aid in determining the constraints on the relative concentrations of different tiles. As described in the SI, for a QC8 with octagonal symmetry we find the following constraint for the partial area fractions Σ , σ , and τ , associated with the large S2 squares, small S1 squares, and the triangles that make up H1, respectively:

$$\Sigma + (3 + 2\sqrt{2})\sigma - \tau = 0. \quad (4)$$

Additionally, since the entire area must be occupied by tiles, these area fractions must satisfy $\Sigma + \sigma + \tau = 1$. Since we know the composition of each tile in our binary mixture, it is straightforward to

rewrite these constraints in terms of the fraction of small particles x_S , yielding:

$$\Sigma = \frac{2(4 + 3\sqrt{2})x_S - 4\sqrt{2} - 5}{6 - 4x_S} \quad (5)$$

$$\sigma = \frac{-(4 + \sqrt{2})x_S + 4}{6 - 4x_S} \quad (6)$$

$$\tau = \frac{-(8 + 5\sqrt{2})x_S + 4\sqrt{2} + 7}{6 - 4x_S} \quad (7)$$

In Fig. 5, we plot this prediction together with the measured tile concentrations in our self-assembled configurations of 10000 particles. Note that in the analysis of the simulation data, we consider only the portion of the system covered by the three valid types of tiles and omit all defects. We find that the observed tile concentrations are essentially independent of size ratio and packing fractions within the investigated regime. Considering the fact that the analyzed configurations were the result of spontaneous self-assembly, and hence contain significant amounts of defects, the agreement is excellent, demonstrating that the system indeed favors tile compositions that correspond to an eight-fold quasicrystalline symmetry.

Finally, in order to quantitatively assess the quality of the quasiperiodic order, we measure the perpendicular strain (also

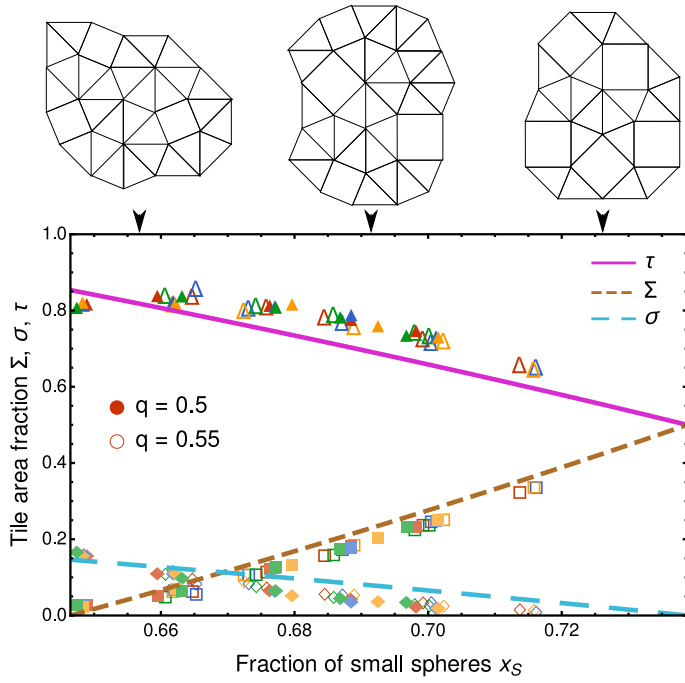


Fig. 5 Area fractions of the three different tiles in the QC8 tiling, Σ , σ , and τ , corresponding to the large squares, small squares, and triangles, respectively. The lines indicate the theoretical prediction on the assumption of a maximally symmetric and globally uniform eight-fold tiling with no defects. Points correspond to simulation results at size ratios $q = 0.5$ (full symbols) and $q = 0.55$ (open symbols). Different colors of points correspond to different packing fractions, with $0.855 \leq \eta \leq 0.87$ for $q = 0.5$ and $0.835 \leq \eta \leq 0.85$ for $q = 0.55$. For the simulation data, we only consider the area covered by non-defect tiles when calculating the composition x_S and the tile area fractions. At the top, three patches illustrate the evolution of the tilings with the composition. From left to right: primarily small squares, mixture of small and large squares and primarily large squares.

often called phason strain⁵⁹ *) of the self-assembled structures. To this end, we associate each vertex in the tilings obtained at the end of the simulations to points in 4D spaces; a procedure known as *lifting*^{61,62}. Dodecagonal and octagonal tilings are lifted to two different 4D spaces whose basis vectors are reported in the SI. This assigns to each particle a position in the 4D superlattice associated with the 2D quasicrystal. This position can then be projected either back to its 2D parallel-space position \mathbf{r}_i^{\parallel} or its 2D perpendicular-space position \mathbf{r}_i^{\perp} . The *parallel* and *perpendicular* sub-spaces are orthogonal to each other, with the parallel sub-space corresponding to the real space of our original quasicrystal lattice. The perpendicular strain is then measured from the relation between points separation in these two projections, following Ref. 63. In particular, we examine the behavior of the perpendicular displacement d^{\perp} as a function of d^{\parallel} , where for each pair of particles i and j , $d_{ij}^{\parallel/\perp} \doteq \|\mathbf{r}_i^{\parallel/\perp} - \mathbf{r}_j^{\parallel/\perp}\|$. For large distances in parallel space, the perpendicular displacement increases linearly with the separation in parallel space and its slope is a direct

measure of the average perpendicular strain $\xi = \sqrt{\xi_1^2 + \xi_2^2}$ with $\xi_{1,2}$ the eigenvalues of the full 2×2 perpendicular strain matrix. For a quasicrystal with long range quasiperiodic order, the perpendicular strain is zero. Defective quasicrystals resulting from self-assembly however typically exhibit some residual perpendicular strain, while periodic phases have an intrinsic non-zero perpendicular strain. For all three configurations shown in Fig. 4, we show the behavior of the perpendicular displacement field in Fig. 6, and compare it to the perpendicular displacement of a reference periodic approximant structure (see SI). Clearly, the perpendicular strain in the self-assembled quasicrystals is non-zero, but significantly lower than that in the periodic approximants. In practice, we observe that the value of the measured average perpendicular strains depend significantly on the state point and fitting range, and is sensitive to the defects in our reconstructed tiling. Typically, our self-assembled structures contain long dislocation defects (see SI), which separate regions with significantly different perpendicular displacements. This may be the result of our self-assembly simulations taking place at relatively high pressures. Rather than forming via a single nucleation event, self-assembly of our quasicrystal phases tends to occur via the rapid formation of quasicrystal tiles throughout the simulation box, followed by a much slower relaxation that rearranges these tiles and allows different domains to coalesce⁶⁴. This slow nature of this process means that it is difficult to obtain high-quality quasicrystals. We note that other simulation studies have found much lower perpendicular strain in quasicrystals^{63,65}, but typically by considering clusters of quasicrystal in direct coexistence with a fluid, which likely allows for significantly faster relaxation.

6 Geometrical arguments for quasicrystal stability

The emergence of the QC12 phase in our system can clearly be understood from its stability in the infinite-pressure limit. However, this is not the case for the QC8 phase: in the infinite-pressure limit, we find only periodic phases in the regime where QC8 was found to self-assemble. Hence, an intriguing question remains – is there a way to understand why these octagonal quasicrystals form? As stated, the three tiles that comprise the tiling are the small S1 square, the large S2 square, and the H1 triangle. In order to form the observed tilings, these shapes must have compatible edge lengths on their shared edges. In particular, the shared edges in the observed tilings are between the large square and the long edge of the H1 triangle, and the small square and the short edge of the H1 triangle. As shown in Fig. 7, the long edge of the triangle matches up almost exactly with the edge of a large square for size ratios between 0.5 and 0.6, in the region where we observe the self-assembly of this phase. Similarly, the short edge of the triangle and the small square match exactly for size ratios below $q = 2 - \sqrt{2} \simeq 0.59$. The fact that a QC8 with mainly small squares is not observed at size ratios below $q = 0.45$ can be understood from a packing argument. As shown in the inset of Fig. 7, when q is decreased below $1/2$, the packing fraction of the triangle tile, which makes up the majority of the QC8 phase, decreases rapidly and drops below that of competing phases, such as the simple hexagonal lattice.

* Note that there has been some debate in the literature with respect to the use of the word ‘phason’ when describing quasicrystal properties^{59,60}.

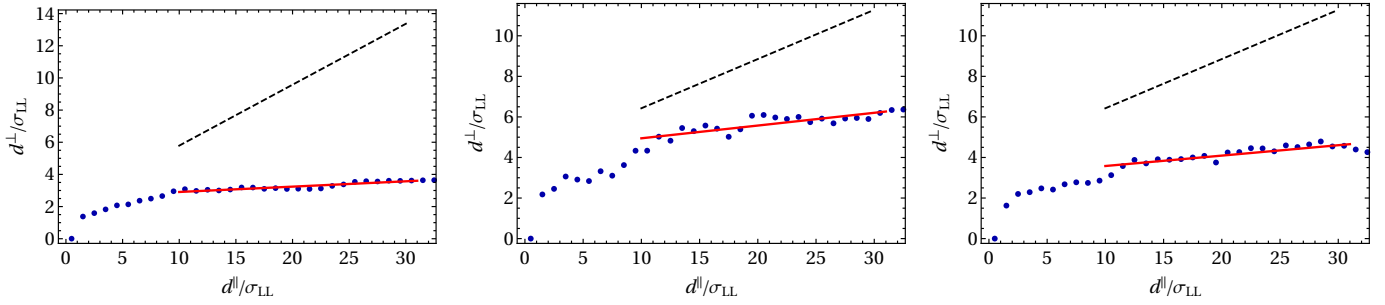


Fig. 6 The average perpendicular displacement d^\perp as a function of the parallel-space displacement d^\parallel for the three self-assembled quasicrystal configurations in Fig. 4. The red lines are linear fits to the large-distance behavior, with the slope related to the average perpendicular strain. For comparison, we also plot the corresponding line for a periodic approximant for each system (dotted black lines).

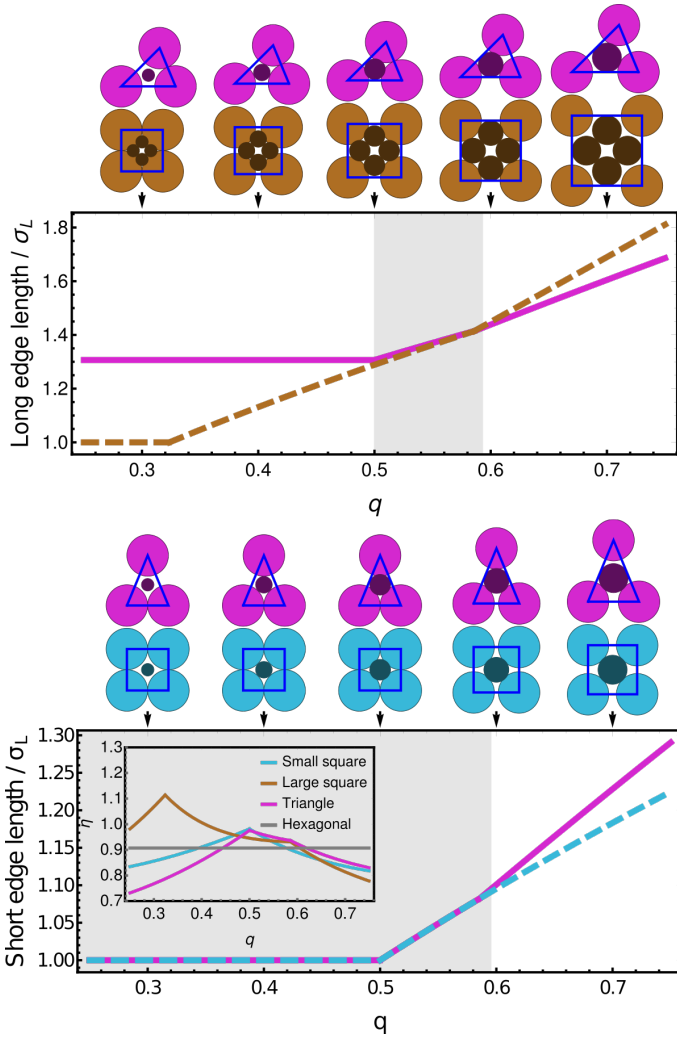


Fig. 7 Evolution of the possible long (top) and short (bottom) edge lengths as a function of size ratio. Matching regions are highlighted with a darker background. For size ratios between 0.5 and 0.6, long edges of the triangle and large square tiles on one hand, and short edges of triangle and small square tiles on the other hand match, thus allowing for the tiles that comprise the octagonal tiling to mix. The inset of the bottom graph displays the packing fraction of the three individual tiles, along with that of a coexistence of hexagonal packings of large and small particles. Self-assembly of QC8 is indeed observed for these values of the size ratio where edge lengths match and tiles pack better than Hex phases.

It is interesting to note that in the case of additive hard disks (or equivalently, spheres whose centers are constrained to a flat plane), we can still observe a regime where the three QC8 tiles match up geometrically, but in this regime their packing fraction is systematically lower than that of a hexagonal lattice (see SI). Consistently, in a self-assembly scan of additive hard disks in this regime we observed no quasicrystal self-assembly. Taken together, these observations suggest that the quasicrystal self-assembly requires both densely packed tiles and geometric edge-matching between them.

7 Discussion

In conclusion, we have explored the self-assembled phases that appear in binary mixtures of hard spheres on a flat plane. In addition to a variety of periodic crystals, we found that this very simple system is capable of forming two different quasicrystal structures: one dodecagonal, commonly observed in soft matter systems, and one octagonal which, to our knowledge, is described here for the first time. The octagonal quasicrystal consists of three distinct tiles, whose relative concentration can be continuously tuned by manipulating the number fraction of small spheres in the mixture, while maintaining the octagonal symmetry. Both observed quasicrystals self-assemble rapidly and reliably over a significant region of parameter space. The tiles proportions in the self-assembled octagonal quasicrystals are in remarkable agreement with theoretical predictions and their stability can be readily understood from geometrical arguments. We note that proving whether these quasicrystal phases are truly thermodynamically stable will require careful free-energy calculations, which we aim to explore in a future study.

In contrast to nearly all other numerical models that have been shown to form 2D quasicrystals, hard spheres on a flat plane can be realized experimentally on the colloidal scale, to the point of quantitative agreement between the experimental hard spheres and their ideal counterparts^{10,43}. The simplicity of the model allows us to identify minimal ingredients for quasicrystal self-assembly: dense tiles with matching edges and entropy alone are sufficient to induce the formation of quasicrystals of different symmetries. Since many colloidal particles include a repulsive spherical core, these simple ingredients might explain quasicrystal formation in a broad range of soft matter systems, beyond hard-sphere colloids alone. This identifies hard spheres on

a plane as a perfect candidate system for tackling fundamental open questions on quasicrystals, such as the dynamics of their nucleation, growth and annealing, the role of their unique phonon excitations or the dynamics of defects, both theoretically and in colloidal experiments on the micron scale.

Conflicts of interest

There are no conflicts to declare.

Acknowledgements

We thank Thomas Fernique, Jean-François Sadoc, Pavel Kalouguine, Alptuğ Ulugöl, and Anuradha Jagannathan for many useful discussions. EF, GF, and FS acknowledge funding from the Agence Nationale de la Recherche (ANR), grant ANR-18-CE09-0025. LF acknowledges funding from the Netherlands Organisation for Scientific Research (NWO) for a Vidi grant (Grant No. VI.VIDI.192.102). The authors acknowledge the use of the Ceres high-performance computer cluster at the Laboratoire de Physique des Solides to carry out the research reported in this article.

Data availability

The data associated with Fig. 3, including all snapshots and scattering patterns, is available as a data package at: <https://doi.org/10.5281/zenodo.7712001>. To help view the data, HTML pages listing the results per size ratio are included.

Notes and references

- 1 B. O'malley and I. Snook, *Phys. Rev. Lett.*, 2003, **90**, 085702.
- 2 U. Gasser, E. R. Weeks, A. Schofield, P. Pusey and D. Weitz, *Science*, 2001, **292**, 258–262.
- 3 B. De Nijs, S. Dussi, F. Smallenburg, J. D. Meeldijk, D. J. Groenendijk, L. Filion, A. Imhof, A. Van Blaaderen and M. Dijkstra, *Nat. Mater.*, 2015, **14**, 56–60.
- 4 D. Wang, T. Dasgupta, E. B. van der Wee, D. Zanaga, T. Altantzis, Y. Wu, G. M. Coli, C. B. Murray, S. Bals, M. Dijkstra *et al.*, *Nat. Phys.*, 2021, **17**, 128–134.
- 5 A. Fortini and M. Dijkstra, *J. Phys. Condens. Matter*, 2006, **18**, L371.
- 6 T. Curk, A. de Hoogh, F. J. Martinez-Veracoechea, E. Eiser, D. Frenkel, J. Dobnikar and M. E. Leunissen, *Phys. Rev. E*, 2012, **85**, 021502.
- 7 G. Jung and C. F. Petersen, *Phys. Rev. Res.*, 2020, **2**, 033207.
- 8 L. Fu, C. Bian, C. W. Shields, D. F. Cruz, G. P. López and P. Charbonneau, *Soft Matter*, 2017, **13**, 3296–3306.
- 9 F. Durán-Olivencia and M. Gordillo, *Phys. Rev. E*, 2009, **79**, 061111.
- 10 A. L. Thorneywork, J. L. Abbott, D. G. Aarts and R. P. Dullens, *Phys. Rev. Lett.*, 2017, **118**, 158001.
- 11 E. P. Bernard and W. Krauth, *Phys. Rev. Lett.*, 2011, **107**, 155704.
- 12 G. Foffi, W. Götze, F. Sciortino, P. Tartaglia and T. Voigtmann, *Phys. Rev. E*, 2004, **69**, 011505.
- 13 E. R. Weeks, J. C. Crocker, A. C. Levitt, A. Schofield and D. A. Weitz, *Science*, 2000, **287**, 627–631.
- 14 E. Zaccarelli, C. Valeriani, E. Sanz, W. Poon, M. Cates and P. Pusey, *Phys. Rev. Lett.*, 2009, **103**, 135704.
- 15 S. Marín-Aguilar, H. H. Wensink, G. Foffi and F. Smallenburg, *Phys. Rev. Lett.*, 2020, **124**, 208005.
- 16 E. Boattini, S. Marín-Aguilar, S. Mitra, G. Foffi, F. Smallenburg and L. Filion, *Nat. Commun.*, 2020, **11**, 1–9.
- 17 S. Pronk and D. Frenkel, *The Journal of Physical Chemistry B*, 2001, **105**, 6722–6727.
- 18 B. van der Meer, F. Smallenburg, M. Dijkstra and L. Filion, *Soft Matter*, 2020, **16**, 4155–4161.
- 19 B. van der Meer, M. Dijkstra and L. Filion, *J. Chem. Phys.*, 2017, **146**, 244905.
- 20 P. N. Pusey and W. Van Megen, *Nature*, 1986, **320**, 340–342.
- 21 A. Yethiraj and A. van Blaaderen, *Nature*, 2003, **421**, 513–517.
- 22 R. P. Dullens, *Soft Matter*, 2006, **2**, 805–810.
- 23 C. P. Royall, W. C. Poon and E. R. Weeks, *Soft Matter*, 2013, **9**, 17–27.
- 24 T. Dotera, *Isr. J. Chem.*, 2011, **51**, 1197–1205.
- 25 D. V. Talapin, E. V. Shevchenko, M. I. Bodnarchuk, X. Ye, J. Chen and C. B. Murray, *Nature*, 2009, **461**, 964–967.
- 26 T. M. Gillard, S. Lee and F. S. Bates, *Proc. Natl. Acad. Sci. U.S.A.*, 2016, **113**, 5167–5172.
- 27 C. Duan, M. Zhao, Y. Qiang, L. Chen, W. Li, F. Qiu and A.-C. Shi, *Macromolecules*, 2018, **51**, 7713–7721.
- 28 F. Lançon, L. Billard and P. Chaudhari, *Europhysics Letters*, 1986, **2**, 625.
- 29 M. Widom, K. J. Strandburg and R. H. Swendsen, *Physical review letters*, 1987, **58**, 706.
- 30 F. Lançon and L. Billard, *Journal de Physique*, 1988, **49**, 249–256.
- 31 M. Widom, D. Deng and C. Henley, *Physical review letters*, 1989, **63**, 310.
- 32 M. N. van der Linden, J. P. Doye and A. A. Louis, *J. Chem. Phys.*, 2012, **136**, 054904.
- 33 M. Zu, P. Tan and N. Xu, *Nature Communications*, 2017, **8**, 1–9.
- 34 P. F. Damasceno, S. C. Glotzer and M. Engel, *J. Phys. Condens. Matter*, 2017, **29**, 234005.
- 35 A. Gemeinhardt, M. Martinsons and M. Schmiedeberg, *EPL*, 2019, **126**, 38001.
- 36 G. Malescio and F. Sciortino, *J. Mol. Liq.*, 2021, 118209.
- 37 E. G. Noya, C. K. Wong, P. Llombart and J. P. K. Doye, *Nature*, 2021, **596**, 367–371.
- 38 P. K. Bommineni, N. R. Varela-Rosales, M. Klement and M. Engel, *Phys. Rev. Lett.*, 2019, **122**, 128005.
- 39 J. Wang, C. F. Mbah, T. Przybilla, B. Apeleo Zubiri, E. Spiecker, M. Engel and N. Vogel, *Nat. Commun.*, 2018, **9**, 1–10.
- 40 T. Dotera, T. Oshiro and P. Ziherl, *Nature*, 2014, **506**, 208–211.
- 41 H. Pattabhiraman, A. P. Gantapara and M. Dijkstra, *J. Chem. Phys.*, 2015, **143**, 164905.

- 42 X. Ye, J. Chen, M. E. Irrgang, M. Engel, A. Dong, S. C. Glotzer and C. B. Murray, *Nature Materials*, 2017, **16**, 214–219.
- 43 A. L. Thorneywork, R. Roth, D. G. Aarts and R. P. Dullens, *J. Chem. Phys.*, 2014, **140**, 161106.
- 44 E. Feyn, A. Jagannathan, G. Foffi and F. Smallenburg, *J. Chem. Phys.*, 2020, **152**, 204901.
- 45 C. Likos and C. Henley, *Phil. Mag. B*, 1993, **68**, 85–113.
- 46 L. Fillion and M. Dijkstra, *Phys. Rev. E*, 2009, **79**, 046714.
- 47 G. Blind, *J. Reine Angew. Math.*, 1969, **1969**, 145–173.
- 48 M. Oxborrow and C. L. Henley, *Phys. Rev. B*, 1993, **48**, 6966.
- 49 M. Impérator-Clerc, A. Jagannathan, P. Kalugin and J.-F. Sadoc, *Soft Matter*, 2021, **17**, 9560–9575.
- 50 D. C. Rapaport and D. C. R. Rapaport, *The art of molecular dynamics simulation*, Cambridge university press, 2004.
- 51 F. Smallenburg, *Euro. Phys. J. E*, 2022, **45**, 22.
- 52 A. Haji-Akbari, M. Engel, A. S. Keys, X. Zheng, R. G. Petschek, P. Palfy-Muhoray and S. C. Glotzer, *Nature*, 2009, **462**, 773–777.
- 53 A. Haji-Akbari, M. Engel and S. C. Glotzer, *Phys. Rev. Lett.*, 2011, **107**, 215702.
- 54 D. Divincenzo and P. J. Steinhardt, *Quasicrystals: the State of the Art*, World scientific, 1991, vol. 11.
- 55 R. Ammann, B. Grünbaum and G. C. Shephard, *Discrete Comput. Geom.*, 1992, **8**, 1–25.
- 56 F. Beenker, *Algebraic theory of non-periodic tilings of the plane by two simple building blocks : a square and a rhombus*, Eindhoven University of Technology, 1982.
- 57 Y. Watanabe, M. Ito and T. Soma, *Acta Crystallogr. A*, 1987, **43**, 133–134.
- 58 T. Fernique, A. Hashemi and O. Sizova, *Discrete Comput. Geom.*, 2021, **66**, 613–635.
- 59 M. de Boissieu, *Phil. Mag.*, 2006, **86**, 1115–1122.
- 60 C. Henley, M. De Boissieu and W. Steurer, *Phil. Mag.*, 2006, **86**, 1131–1151.
- 61 P. R. Baake M., Grimm U., *Aperiodic Order: Volume 1, A Mathematical Invitation*, Cambridge University Press, 2013.
- 62 M. Baake, D. Eciija and U. Grimm, *Z. Kristallogr. Cryst. Mater*, 2016, **231**, 507–515.
- 63 K. Je, S. Lee, E. G. Teich, M. Engel and S. C. Glotzer, *Proc. Natl. Acad. Sci. U.S.A.*, 2021, **118**, e2011799118.
- 64 W. Steurer, *Z. Anorg. Allg. Chem.*, 2011, **637**, 1943–1947.
- 65 M. Engel, P. F. Damasceno, C. L. Phillips and S. C. Glotzer, *Nat. Mater.*, 2015, **14**, 109–116.

Supplemental information: Self-assembly of dodecagonal and octagonal quasicrystals in hard spheres on a plane

E. Fayen, M. Impérator-Clerc, L. Filion, G. Foffi, F. Smallenburg

FINAL CONFIGURATIONS

An archive of simulated final configurations for the data set depicted in Figure 3 of the main text is provided at <https://doi.org/10.5281/zenodo.7712001> via Zenodo. In particular, we provide a zipped archive of the final configurations, snapshot images, and diffraction patterns for all simulations performed using $N = 2000$ particles. The files are organized into folders and accompanied by HTML documents which allow for a rapid visualization of all simulation results for a single size ratio.

HEX_L⁺ PHASE AT DIFFERENT COMPOSITIONS

As mentioned in the main text, we use the label Hex_L⁺ to refer to any phase consisting of a hexagonal lattice of large spheres interspersed with small spheres, regardless of the ordering of the smaller spheres. In Fig. 1, we show snapshots for a range of different compositions. The hexagonal symmetry of the large-sphere lattice remains in place even though the concentration of small spheres varies drastically. For low compositions x_S , only a few small spheres are randomly interspersed in the triangular holes in the lattice. This concentration increases all the way up to $x_S \simeq 2/3$, at which point all triangular holes in the lattice are filled, corresponding to the T1 crystal phase. Above this concentration, the large particles start to become more separated, as additional small particles fill the gaps between them. While this leads to local lattice distortions and a decrease in hexagonal ordering (e.g. at $x_S = 0.7$), overall the system maintains its hexagonal symmetry. In principle, pushing these systems to larger packing fractions may stabilize more ordered phases, such as those predicted by the infinite-pressure phase diagram in the main text. However, these high-density phases are likely hard to reach via spontaneous self-assembly due to the kinetic arrest that occurs at high packing fractions.

TILING ANALYSIS

The quasicrystalline phases can be rationalised as tilings of the plane by decorated tiles. To identify the underlying tiling in simulation snapshots, we first create bonds between all large particles within a cutoff distance of $1.3\sigma_{LL}$ for QC12 and $1.7\sigma_{LL}$ for QC8 systems. Since the QC8 contains short and long bonds, the long cutoff distance required to capture long bonds also generates crossing bonds within S1 tiles, which need to be removed. Tiles are then reconstructed from cycles in the bond network, and sorted by shape and orientation.

To characterise the neighbour network, we compute the bonds length and angle distributions, as shown in Figure 2. Bond angles are relative to the horizontal. In the vicinity of the QC8 region, the bond length distribution is clearly bimodal. A cutoff is set at the minimum of the distribution in-between the two peaks, which discriminates between long and short bonds. Since the cutoff value can vary slightly with the composition and packing fraction of the system, we determine it automatically for each snapshot. The bond angle distribution exhibits 16 sharp peaks centered on the directions of an ideal tiling of large squares, small squares and equilateral triangles. Correlating the orientation with the bond length shows that short and long bonds each follow a distinct set of 8 orientations, offset by $\pi/8$.

TILES FRACTIONS IN QC8

For the square-triangle tiling associated with the QC12 phase, it is well known that global twelve-fold symmetry only occurs under the condition that the two area fractions of the tiling covered by squares and triangles are the same and equal to $1/2$ [1, 2]. Here, we determine under what conditions the QC8 phase can exhibit 8-fold symmetry. To this end, we consider a QC8 tiling consisting of large squares S , small squares s , and triangles T , with long edge length a . Counting the different orientations, this results in a total of 12 different tiles: two orientations of both types of squares, and 8 orientations of the triangles. These are listed in Table I. We then consider an infinite, globally

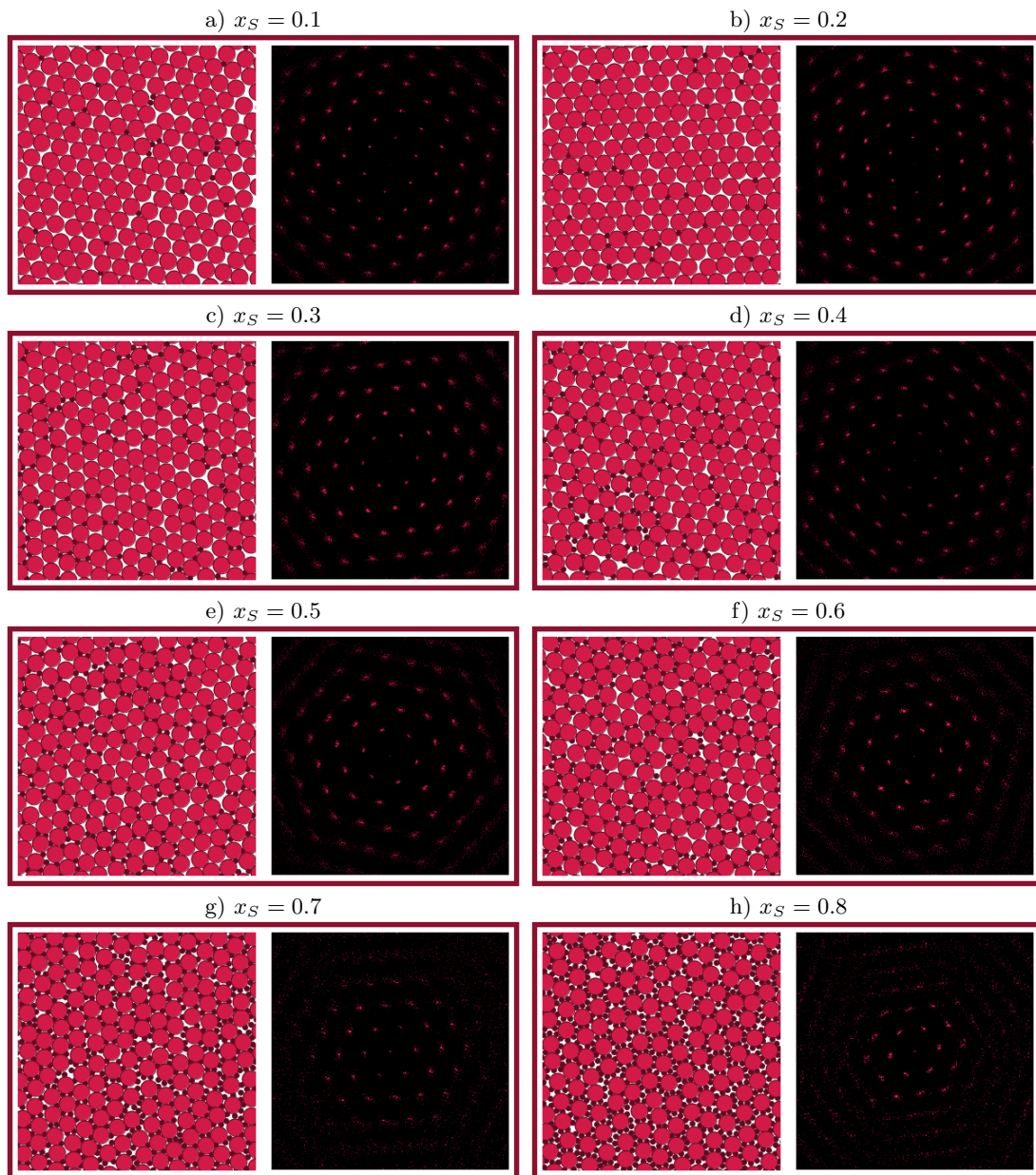


FIG. 1. Variations of the Hex_L^+ phase, at size ratio $q = 0.35$ and varying compositions x_S . The packing fractions for the snapshots vary from $\eta = 0.82$ in (a) to $\eta = 0.96$ in (h), in steps of 0.02.

uniform[2] tiling consisting of a mixture of these tiles, with the area fraction covered by each tile type denoted as Σ_i for the large squares, σ_i for the small squares, and τ_i for the triangles, where i denotes the orientation of the tile.

The first obvious constraint on our tiling is that it should cover the entire plane. Hence, the area fractions must satisfy

$$\Sigma + \sigma + \tau = 1, \quad (1)$$

where $\Sigma = \sum_i \Sigma_i$, $\sigma = \sum_i \sigma_i$, and $\tau = \sum_i \tau_i$.

One set of constraints on these tile concentrations follows from the simple observation that each edge must have an opposing partner. Considering, for example, the short edge in triangle T_1 , this leads to the constraint that

$$n_{T_1} + n_{s_1} = n_{T_5} + n_{s_1}, \quad (2)$$

with n_{X_i} denotes the number of tiles of type X_i . This trivially implies that $\tau_1 = \tau_5 = \tau_{15}/2$, and likewise it can be shown that $\tau_2 = \tau_6 = \tau_{26}/2$, $\tau_3 = \tau_7 = \tau_{37}/2$, and $\tau_4 = \tau_8 = \tau_{48}/2$.

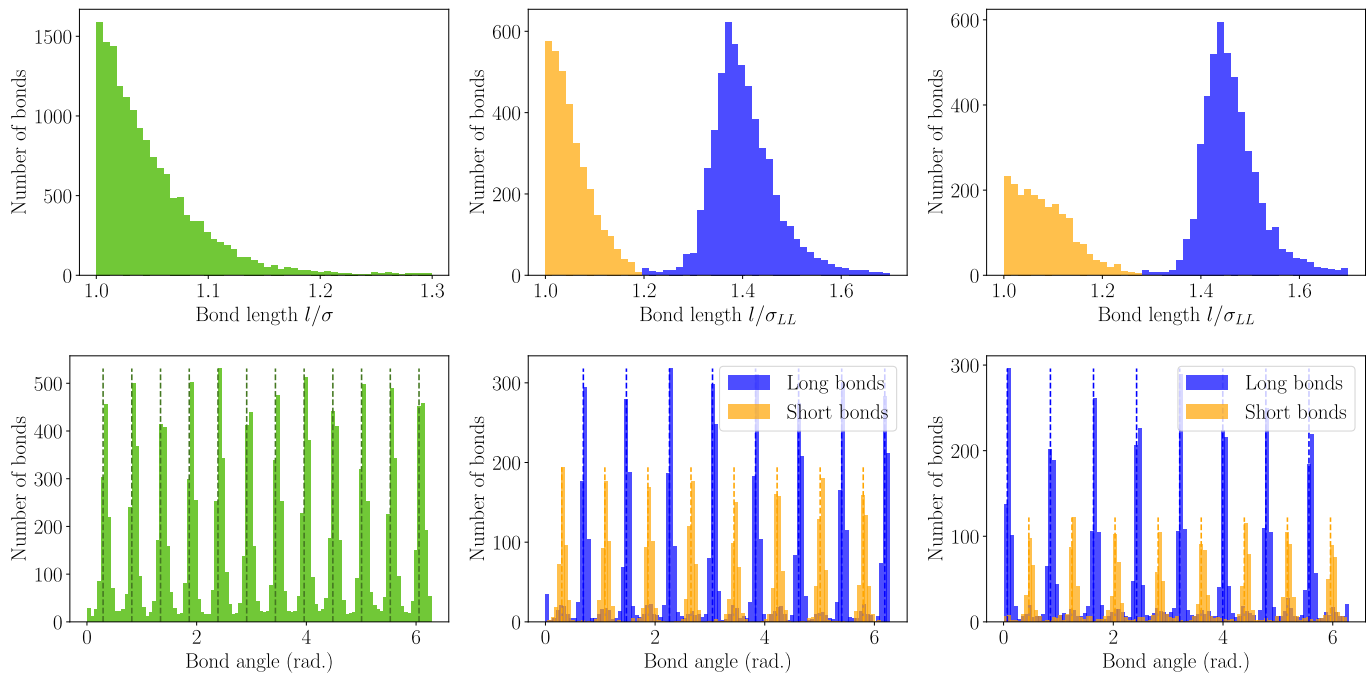


FIG. 2. Neighbour bonds characterisation in systems of 10^4 non-additive hard disks, with size ratio $q = 0.45$, composition $x_S = 0.35$ and packing fraction $\eta = 0.84$ (Left), $q = 0.5$, $x_S = 0.675$, $\eta = 0.86$ (Centre) and $q = 0.55$, $x_S = 0.725$, $\eta = 0.84$ (Right). The first system forms a dodecagonal random tiling quasicrystal, while the two last ones form octagonal random tiling quasicrystals. (Top) Bonds length distributions show a clear distinction between short and long bonds in octagonal tilings. (Bottom) Bond angle distributions.

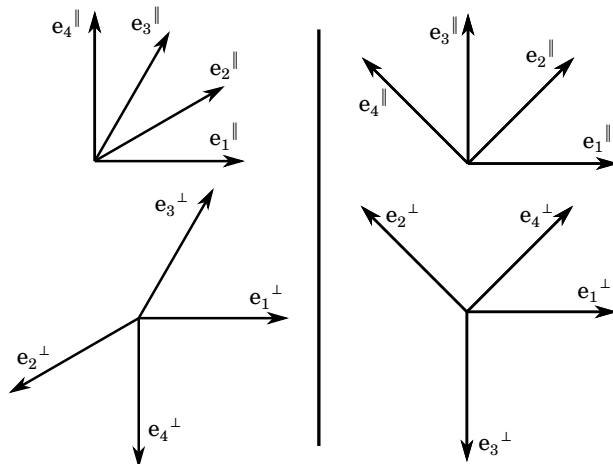


FIG. 3. Projections of the 4D lift vectors on the parallel and perpendicular sub-spaces for the square-triangle (Left) and large square-small square-isosceles triangle (Right) tilings.

Another constraint on the various tile concentrations can be obtained by using the four-dimensional representation of the tilings. For this, we follow the procedure outlined in e.g. [1–3]. In particular, in the QC8 tiling, each long edge can only lie along one of 4 different orientations \mathbf{e}_1 through \mathbf{e}_4 , illustrated in Fig. 3(left). Short edges can then be constructed by taking the difference between two of these vectors (e.g. $\mathbf{e}_2 - \mathbf{e}_1$). As a result, each vertex in our tiling can be written as a linear combination of an integer number of the four vectors \mathbf{e}_i , and hence can be seen as a point on a four-dimensional lattice. We then associate each vector \mathbf{e}_i with a corresponding vector \mathbf{e}_i^\perp , illustrated in Fig. 3(right), such that each vertex in the tiling can be uniquely associated with a point in the perpendicular space [3, 4].

We can then consider a mapping $\phi(\mathbf{r})$ that maps each vertex in our original tiling to its corresponding point in the perpendicular space. Within each tile, $\phi(\mathbf{r})$ is a linear interpolation between the mapped vertices of that tile. Hence, ϕ is a continuous, piecewise linear function, with a constant hyperslope within each tile. The hyperslope within one


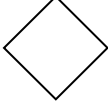
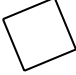
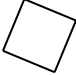

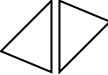


Name	Tile	Area A_{X_i}	Hyperslope B_{X_i}	$\det B_{X_i}$
S_1		a^2	$\begin{pmatrix} 1 & 0 \\ 0 & -1 \end{pmatrix}$	-1
S_2		a^2	$\begin{pmatrix} -1 & 0 \\ 0 & 1 \end{pmatrix}$	-1
s_1		$(2 - \sqrt{2})a^2$	$(1 + \sqrt{2}) \begin{pmatrix} 0 & -1 \\ -1 & 0 \end{pmatrix}$	$-3 - 2\sqrt{2}$
s_2		$(2 - \sqrt{2})a^2$	$(1 + \sqrt{2}) \begin{pmatrix} 0 & 1 \\ 1 & 0 \end{pmatrix}$	$-3 - 2\sqrt{2}$
$T_{1,5}$		$\frac{1}{2\sqrt{2}}a^2$	$\begin{pmatrix} 1 & -2 \\ 0 & 1 \end{pmatrix}$	1
$T_{2,6}$		$\frac{1}{2\sqrt{2}}a^2$	$\begin{pmatrix} -1 & 0 \\ 2 & -1 \end{pmatrix}$	1
$T_{3,7}$		$\frac{1}{2\sqrt{2}}a^2$	$\begin{pmatrix} -1 & 0 \\ -2 & -1 \end{pmatrix}$	1
$T_{4,8}$		$\frac{1}{2\sqrt{2}}a^2$	$\begin{pmatrix} 1 & 2 \\ 0 & 1 \end{pmatrix}$	1

TABLE I. Summary of the 12 different tiles comprising the QC8 tiling. The third column reports the area of each tile, assuming that large squares have edges of length a . The fourth column contains the constant hyperslope of each tile, *i.e.* the 2x2 matrix that maps points inside that tile in the original tiling to the perpendicular space. The last column displays the determinant of the hyperslope for each tile, which is used to obtain Eq 6.

tile is completely determined by the vectors that form it. Hence, tiles of the same type and orientation have the same hyperslope. Specifically, within a tile X_i , the hyperslope B_{X_i} is given by:

$$B_{X_i} = \begin{pmatrix} \frac{\partial \phi_x}{\partial x} & \frac{\partial \phi_x}{\partial y} \\ \frac{\partial \phi_y}{\partial x} & \frac{\partial \phi_y}{\partial y} \end{pmatrix}. \quad (3)$$

In Table I, we report the hyperslope for each of the 12 tiles in the QC8 tiling.

In a globally uniform tiling, over long distances \mathbf{r} , $\phi(\mathbf{r})$ has a well-defined average hyperslope B (also known as the global perpendicular strain), which can be written as the weighted sum of the hyperslopes of the individual tiles [2]:

$$B = \sum_{i=1}^2 \Sigma_i B_{S_i} + \sum_{i=1}^2 \sigma_i B_{s_i} + \sum_{i=1}^8 \tau_i B_{T_i}. \quad (4)$$

Following Ref. [2], uniformity of the tiling then imposes that

$$\sum_{i=1}^2 \Sigma_i \det B_{S_i} + \sum_{i=1}^2 \sigma_i \det B_{s_i} + \sum_{i=1}^8 \tau_i \det B_{T_i} = \det B. \quad (5)$$

Using the matrices listed in Table I, this leads to the following constraint:

$$\Sigma + (3 + 2\sqrt{2})\sigma - \tau = (\Sigma_1 - \Sigma_2)^2 + (3 + 2\sqrt{2})(\sigma_1 - \sigma_2)^2 - \tau^2 + (2 + 2\sqrt{2})(\tau_{15} - \tau_{26} + \tau_{37} - \tau_{48})(\sigma_1 - \sigma_2) + 8(\tau_{15}\tau_{37} + \tau_{26}\tau_{48}). \quad (6)$$

This constraint can be regarded as the equivalent of the Nienhuis relation [2, 5] for the (QC12) square-triangle tiling, but for our QC8 tiling.

For a maximally symmetric tiling with eight-fold symmetry, the requirement is that all orientations of each tile appear in the same amount [2]. In other words:

$$\Sigma_1 = \Sigma_2 = \frac{\Sigma}{2} \quad (7)$$

$$\sigma_1 = \sigma_2 = \frac{\sigma}{2} \quad (8)$$

$$\tau_{15} = \tau_{26} = \tau_{37} = \tau_{48} = \frac{\tau}{4}. \quad (9)$$

When we impose this, the average hyperslope B vanishes (zero perpendicular strain), and as a result the right-hand side of Eq. 6 similarly becomes zero, yielding:

$$\Sigma + (3 + 2\sqrt{2})\sigma - \tau = 0. \quad (10)$$

Finally, we can express the area fractions Σ , σ and τ in terms of the particle composition x_S by using the known composition of each tile, combined with equations 1 and 10 (see equations 3, 4 and 5 of the main text).

LIFT TO 4D AND PERPENDICULAR STRAIN

Mapping a tiling to its higher dimensional representation is called *lifting*. This procedure gives access to valuable information for the analysis of quasicrystals. In particular, the relationship between the distances in perpendicular and parallel projections can be used to measure the perpendicular strain of the structure at hand.

In practice, lifting a structure amounts to assigning each vertex to a points in a higher dimensional space. The lift spaces of both square-triangle and large square-small square-isosceles triangle tilings are 4-dimensional, but with different basis vectors. In Figure 3, we report the parallel and perpendicular projections of the lift vectors used to analyse our tilings. We use the standard lift basis for the square-triangle tiling [2]. The vectors used to lift the large square-small square-isosceles triangle tilings are the those commonly used for lifting the Ammann-Beenker or Watanabe-Ito-Soma tilings [6, 7].

After reconstruction of the tilings, we lift the tiling recursively from a starting point, tile after tile. We find that lifting the tiling tile after tile rather than bond after bond is more robust. Indeed, we lift only tiles that unambiguously correspond to one of the allowed orientation, thus preventing the ambiguous orientation of a single bond to propagate further in the recursive lifting. During the lift construction, we ignore the periodic boundary conditions of the simulation box.

Once a tiling is lifted, projecting back onto the parallel subspace yields a “rectified” tiling with no thermal noise, where all tiles have their ideal shape as illustrated in Figure 4-top. The rectified tilings contain small defects that are local and do not disrupt the tiling further away, as well as long defect lines that nucleate at topological defects and separate islands of tiling. Interestingly these “tears” defects were previously observed by Joseph and Elser in a simple growth model for the QC12 tiling of squares and triangles [8]. One can also project the lifted vertices to the perpendicular subspace 4-bottom. The perpendicular projection gives indication about the quality of the quasicrystal. In an ideal dodecagonal quasicrystal, the vertices form a fractal-shaped pattern with 12-fold symmetry. In a random tiling quasicrystal, this shape is blurred somewhat, but remains compact. Here, because of the many defects in the tiling, we observe that the points spread away from the origin. Nonetheless, we note that the perpendicular projections form a very dense cluster (note the different scales for perpendicular and parallel axis), a signature of quasicrystalline structures.

With both parallel and perpendicular coordinates of each vertex, we can compute the perpendicular strain of the self-assembled tilings. By binning the pair particle distances in parallel space, we compute the perpendicular displacement field as explained in the main text [9], and measure the average perpendicular strain ξ as the slope of the linear regime, as illustrated in the main text. We compare these average perpendicular strains with those of reference periodic structures. For the square-triangle tilings, we take the first approximant to the dodecagonal quasicrystal (the sigma phase, see Figure 5-Left) as a reference structure of average perpendicular strain $\xi_{\text{ref}} = 2\sqrt{2} - \sqrt{6} \approx 0.38$. For the large square-small square-isosceles triangle tilings, we use a square lattice decorated with octagons as our reference periodic structure. The octagon can host various clusters as depicted in Figure 5-Right thus allowing to construct periodic structures with different tiles concentrations. This family of periodic structure all have an average perpendicular strain of $\xi_{\text{ref}} = 3\sqrt{2} - 4 \approx 0.24$.

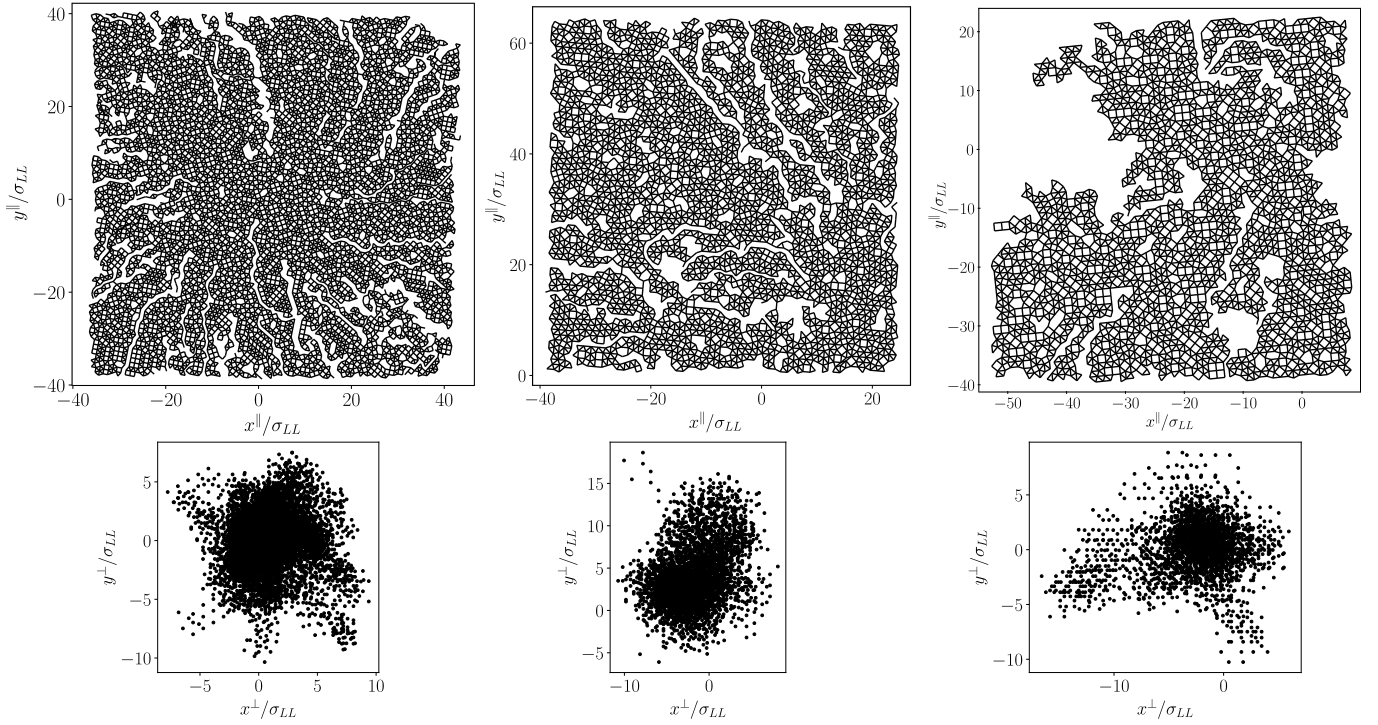


FIG. 4. Parallel (Top) and perpendicular (Bottom) projections of the lifted tilings. (Left) QC12 $q = 0.45$, $x_S = 0.35$, $\eta = 0.84$. (Centre) QC8 $q = 0.5$, $x_S = 0.675$, $\eta = 0.86$. (Right) QC8 $q = 0.55$, $x_S = 0.725$, $\eta = 0.84$. The empty region in to top right corner corresponds to a fluid pocket with no tiling structure.

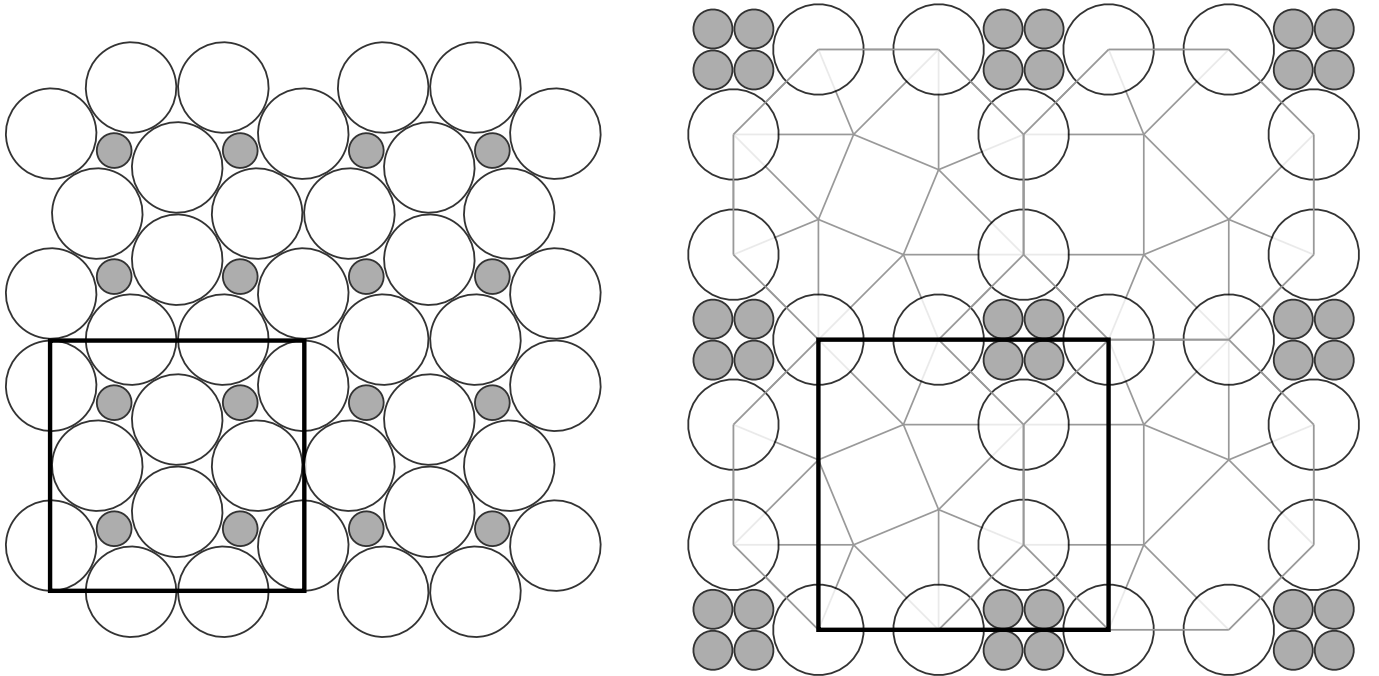


FIG. 5. Reference periodic phases. Black squares highlight the unit cells. (Left) The sigma phase, first approximant of the dodecagonal tiling. (Right) A reference periodic structure based on the large square-small square-isosceles triangle tiling. The octagons can host cluster of variable composition and orientation. Possible fillings are suggested in grey.

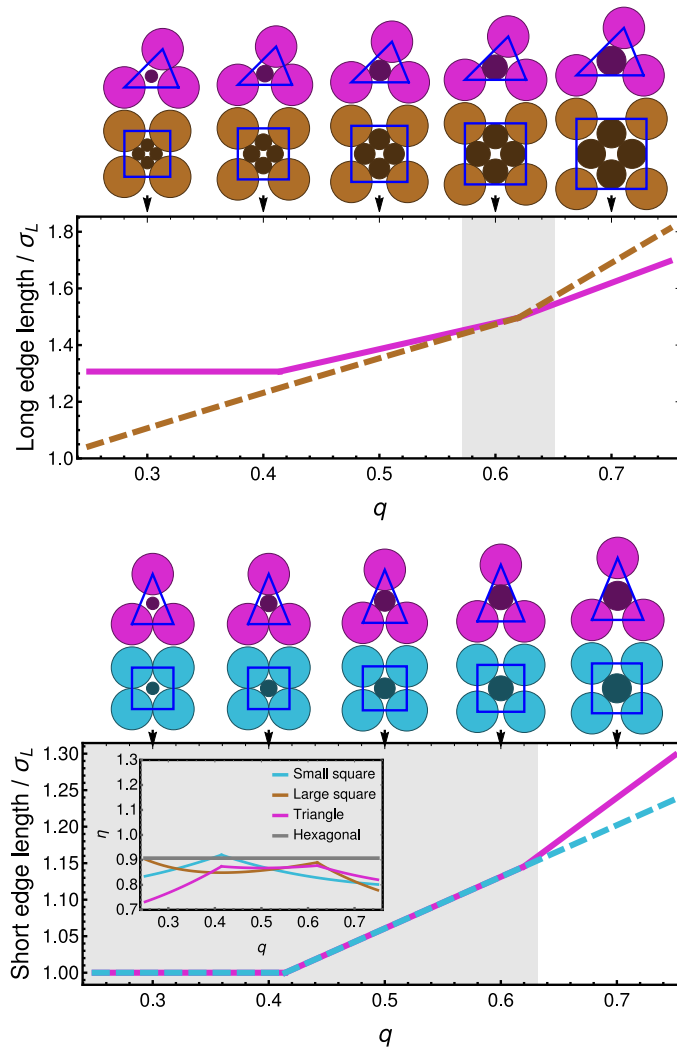


FIG. 6. Comparison of the long (top) and short (bottom) edge length of the tiles expected to form an octagonal quasicrystal in binary mixtures of *additive* hard disks. Size ratio intervals for which long or short edges match are highlighted with a darker background. The inset in the bottom graph displays the packing fraction of the various tiles as a function of size ratio, along with that of hexagonal packings.

ADDITIVE CASE

In complement to the main text analysis of spheres on a plane, which correspond to non-additive hard disks, we examine here the geometrical constraints in mixtures of *additive* hard disks, which cannot overlap (i.e., the non-additivity parameter is $\Delta = 0$). The 3D equivalent of this system would consist of spheres whose centers are constrained to lie in the same plane. Figure 6 shows the short and long edge lengths of the square and triangle tiles that can be formed with additive hard disks. While edge lengths could match for size ratios around $q = 0.6$, the inset graph shows that in this regime, the packing fraction of the tiles is systematically lower than that of hexagonal packing of large and small disks suggesting that the tiles are not dense enough to be stable in this system.

This observation was confirmed by simulating binary additive hard disk mixtures for size ratios between $q = 0.4$ and $q = 0.6$ in steps of 0.05, packing fractions between $\eta = 0.7$ and 0.9 in steps of 0.02, and compositions ranging from $x_S = 0.6$ to 0.9 in steps of 0.05. Quasicrystal self-assembly was observed in none of these simulations, although we cannot exclude the possibility of QC8 formation in longer simulation or different parameter regimes. As suggested by the above packing argument, many of the systems instead had a tendency to demix into separate large and small hexagonal domains. This is also consistent with the sparsity of stable binary crystal structures found at infinite

pressure for additive hard disks in this regime [10, 11].

- [1] M. Oxborrow and C. L. Henley, Random square-triangle tilings: A model for twelfefold-symmetric quasicrystals, *Phys. Rev. B* **48**, 6966 (1993).
- [2] M. Impéror-Clerc, A. Jagannathan, P. Kalugin, and J.-F. Sadoc, Square-triangle tilings: an infinite playground for soft matter, *Soft Matter* **17**, 9560 (2021).
- [3] M. Baake, D. Eciija, and U. Grimm, A guide to lifting aperiodic structures, *Z. Kristallogr. Cryst. Mater* **231**, 507 (2016).
- [4] M. Zu, P. Tan, and N. Xu, Forming quasicrystals by monodisperse soft core particles, *Nature Communications* **8**, 1 (2017).
- [5] B. Nienhuis, Exact solution of random tiling models, *Phys. Rep.* **301**, 271 (1998).
- [6] R. Ammann, B. Grünbaum, and G. C. Shephard, Aperiodic tiles, *Discrete Comput. Geom.* **8**, 1 (1992).
- [7] Y. Watanabe, M. Ito, and T. Soma, Nonperiodic tessellation with eightfold rotational symmetry, *Acta Crystallogr. A* **43**, 133 (1987).
- [8] D. Joseph and V. Elser, A Model of Quasicrystal Growth, *Phys. Rev. Lett.* **79**, 1066 (1997).
- [9] K. Je, S. Lee, E. G. Teich, M. Engel, and S. C. Glotzer, Entropic formation of a thermodynamically stable colloidal quasicrystal with negligible phason strain, *Proc. Natl. Acad. Sci. U.S.A.* **118**, e2011799118 (2021).
- [10] C. Likos and C. Henley, Complex alloy phases for binary hard-disc mixtures, *Phil. Mag. B* **68**, 85 (1993).
- [11] E. Fayen, A. Jagannathan, G. Foffi, and F. Smallenburg, Infinite-pressure phase diagram of binary mixtures of (non) additive hard disks, *J. Chem. Phys.* **152**, 204901 (2020).